

Article

Influence of Fine Crystal Percentage on the Electrical Properties of ZnO Ceramic-Based Varistors

Abdullah Aljaafari ^{1,*}  and Ahmed Sedky ²¹ Department of Physics, College of Science, King Faisal University P.O. Box 400, Al-Ahsa 31982, Saudi Arabia² Physics Department, Faculty of Science, Assiut University, Assiut 71511, Egypt; sedky1960@yahoo.com

* Correspondence: aaljaafari@kfu.edu.sa

Received: 6 July 2020; Accepted: 4 August 2020; Published: 6 August 2020



Abstract: Herein, the effect of nanocrystal percentage in bulk-ZnO varistors was studied. The structure of ZnO nanocrystals was examined using X-ray diffraction (XRD) and field-emission scanning electron microscopy (FE-SEM). The XRD studies showed that the nanocrystals were indexed with the hexagonal wurtzite structure of ZnO nanostructures. The average crystallite size deduced from XRD analysis ranged between 135 and 273 nm, eight-fold lower than that of the nanoparticles observed in FE-SEM micrographs (1151–2214 nm). The percentage of nanocrystals added into the ZnO varistor was increased from 0 to 100%. Electrical measurements (I – V profiles) showed that the non-linear region, breakdown field, and activation energy were found to decrease with the addition of ZnO fine crystals up to 10% and then increased upon a further increase in fine crystals. However, the electrical conductivity measured at room temperature was improved, and the highest value of 2.11×10^{-5} was observed for 10% fine crystals and then decreased upon a further increase in the fine crystal concentration in bulk ZnO. The breakdown field decreased with the increase in the percentage of ZnO nanostructures in the varistor up to 10% and then increased upon the further addition of ZnO nanostructures. The nonlinear coefficient (α) was decreased from 18.6 for bulk ZnO and remained close to unity for the samples that contained fine crystals. The electrical conductivity was generally improved with the increase in the concentration of the ZnO fine crystals. The activation energy was found to be 128, 374, and 815 meV for the bulk samples and 164, 369, and 811 meV for the samples that contained 100% fine crystals for the three temperature regions of 300–420, 420–580, and 580–620 K, respectively. These results will provide a pathway toward the determination of a correlation between the electrical and microstructural properties of ZnO-based varistors for future device applications.

Keywords: ZnO nanocrystals; ZnO varistor; breakdown field; nonlinear I – V ; activation energy

1. Introduction

Over the past decades, ZnO has been used in various applications including varistors, transparent electrodes, gas sensors, and photocatalysis [1–8]. ZnO polycrystalline nanostructures show nonlinear I – V characteristics due to the potential barriers formed at the inter-grain boundaries [9–11]. The formation of the nonlinearity, in parallel with high current densities and breakdown fields, is the most significant property of varistors. The increase in current is more rapid than that in voltage; the I – V curve shows an upturn region at current densities beyond 10^3 A/cm² and breakdown fields (≤ 5000 V/cm). This upturn region indicates that the voltage drops at the grains and controls ZnO for varistor applications. Generally, the nonlinearity phase depends on the density, chemical composition of the compound, and nanostructure development [12–15].

Nanotechnology is of increasing importance in many research branches due to the interesting properties associated with the sizes of small particles [16–18]. Although the bulk ZnO material is well known for having a wurtzite hexagonal structure, ZnO nanocrystals have different crystalline

structures depending on how they are prepared [19]. It has been reported that the ZnO distributed nanoparticles have an enhanced luminous intensity compared to the ZnO bulk [20]. Moreover, cubic ZnO nanoparticles can be formed by flash evaporation [21]. In addition, it is accepted that fine nanoparticles of face-centered-cubic structure of a few hundred nanometers in size can form multiple nanoparticles with a diamond structure [22–27]. In the last few years, extensive studies on the synthesis, characterization, and physical properties of nanomaterials have been conducted. Enormous research has been focused on metal oxide nanoparticles owing to their unusual properties upon entering the nanoscale regime [28,29].

The electrical characteristics of ZnO ceramic varistors are dependent on their microstructural features as follows: (i) the grain boundaries between the ZnO grains, which have nonlinear current–voltage characteristics with an optimum break-down voltage, can be low—or the grain boundary may not exhibit varistor behavior at all, possess ohmic characteristics, and define the characteristics of the varistor in the pre-break-down region, and (ii) the ZnO grains and their sizes—which define the number of grain boundaries between the electrodes and thus the break-down voltage of the varistor—and their conductivity define the performance of the varistor at high currents in the upturn region of the current–voltage characteristics [30]. Previous studies showed that some dopants have a significant effect on the pre-break-down and the upturn current–voltage characteristics of varistors even with minute amounts of additives. For example, in very small amounts, aluminum is a potential dopant for increasing the conductivity of the ZnO grains and enhancing the varistor’s performance at high currents [31–34]. Various physicochemical properties of ZnO nanostructures can be strongly affected by the presence of deep and shallow defect-related in-gap states, which depend on the material’s growth conditions in a way that is still far from being understood. Thus, a relationship or the effect of the dopant on the electrical properties of ZnO varistors needs to be studied.

However, to the best of our knowledge, the effect of nanocrystals on the characteristics of bulk ZnO varistors and their correlation have not been reported. Therefore, in this work, we studied the effect of increasing the fine crystal amount in the bulk-ZnO varistor on the electrical properties. The variation in the breakdown field (EB) versus fine crystal content is well studied. The electrical conductivity of the bulk and mixed phase ZnO was investigated. The activation energy versus ZnO fine crystal amount was determined. The structure and morphology were characterized by using XRD and FE-SEM techniques.

2. Experimental Details

2.1. Preparation

The experiment was started with raw ZnO (Sigma-Aldrich ZnO powder, <5 μm particle size, 99.9%) with an average crystallite size of 273 nm and particle size of 2214 nm. In advance, ZnO powder was milled (using RETSCH-Planetary Ball milling PM400) for several hours to obtain fine crystals with a size of 144 nm. Then, the samples were prepared by mixing the raw powders with these fine crystals in determined percentages of 0.0, 5, 10, 30, 50, 75, and 100%, using the conventional solid-state reaction method. The obtained mixture was then calcined for 900 °C in air for 12 h. The as-obtained powder was then pressed into a disk (diameter, 1.0 cm, and thickness, 0.3 cm). These disks were sintered for 10 h at 1000 °C in air. The disks were then cooled down to room temperature. The densities of the bulk samples were measured in terms of volume and weight.

2.2. Characterizations

Microstructure analysis of the obtained products was performed using an X-ray diffractometer (XRD-Philips Type PW 1710, Amsterdam, The Netherlands) with $\text{CuK}\alpha$ radiation of 1.5406 Å. The surface morphologies were studied using FE-SEM (FE-SEM-Model JEOL JMS-7000, Peabody, MA, USA). The I – V characteristics were measured with a Keithley meter (Model 6517, Beaverton, OR, USA), DC power supply of 5.0 kV, and digital multimeter. The products were polished well and

inserted into copper electrodes. The current was measured relative to the applied voltage at room temperature. For the electrical contacts, high-quality silver paste was used on the sample surfaces. Then, electrical resistivity ($\rho = (R\ell/A)$) as a function of the temperature measurements was determined in the range of 300–620 K, and the electrical conductivity was calculated ($\sigma = (1/\rho)$). The values of electrical conductivity were used to calculate the activation energy of the considered samples.

3. Results and Discussion

3.1. Structural Analysis of ZnO Nanomaterials

The XRD patterns (Figure 1a–f) show that all the samples exhibited a hexagonal wurtzite crystal structure; no other impurity lines can be observed, implying that the ZnO fine crystal content was 100%. The standard peaks of ZnO (100), (002), (111), (102), (110), (103), (200), and (112) are observed [35–37]. To further confirm whether the ZnO fine crystals were localized for ZnO in the cell, the lattice parameters of the samples were calculated using $c = 2d_{(002)}$, $a = d_{(100)}/(\cos 30^\circ)$ and are listed in Table 1. However, we could not find any significant changes in the lattice parameters a and c with the addition of ZnO fine crystals. The values ranging from 3.20 to 3.22 Å for the lattice parameter a and 5.145 and 5.17 Å for the c parameter are in agreement with the previous data based on ZnO ceramics [36,38]. Additionally, the average crystallite size D_{hkl} was calculated using Scherer's equation [28]:

$$D_{hkl} = k\lambda / (\Delta\theta \cos\theta) \quad (1)$$

where λ is the X-ray wavelength ($\lambda = 1.5418\text{Å}$), $\Delta\theta$ is the half maximum line width, θ is the Bragg angle, and k is a constant ($k = 0.9$ for this type of ceramic). The average crystallite size ($D_{(111)}$) against the percentage of fine crystal content for all the samples is listed in Table 1. It is clear that $D_{(111)}$ was reduced with the addition of fine crystals into the bulk up to 100% with 10% fluctuation. The values of average crystallite size range from 143 to 273 nm for fully raw powder (0.0% sample).

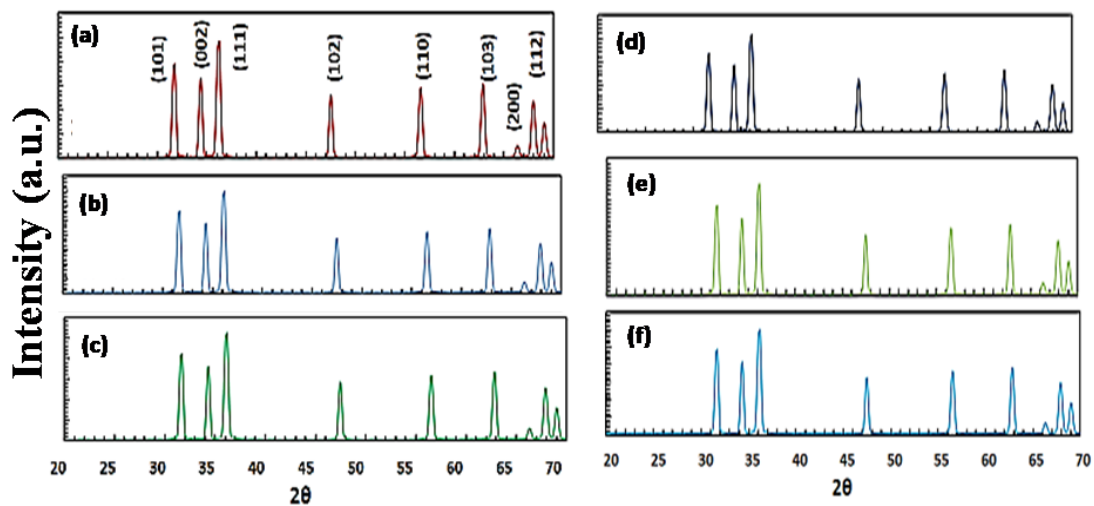
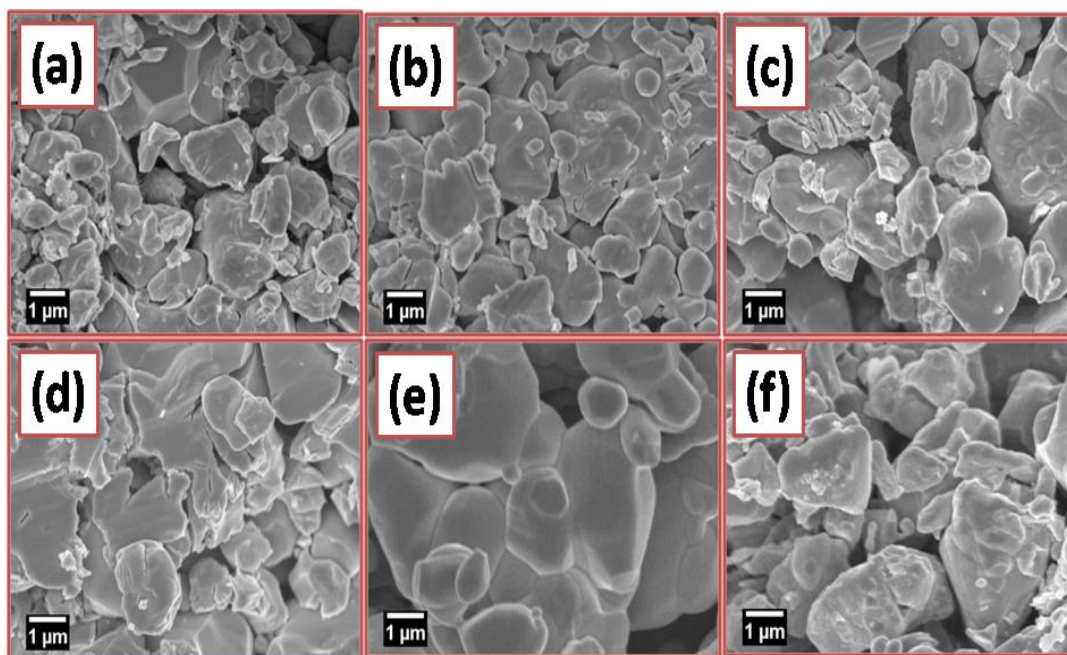


Figure 1. XRD patterns of mixed powder; (a) 0.0, (b) 5, (c) 10, (d) 50, (e) 75, and (f) 100% of fine crystals.

Table 1. Lattice parameters, and average crystallite and particle sizes for ZnO mixed samples.

Fine Crystal Percent	Lattice Parameters		Crystallite Size (nm)	Particle Size (nm)
	A (Å)	C (Å)		
0	3.203	5.145	273	2214
5	3.214	5.149	163	1572
10	3.223	5.163	143	1277
30	3.226	5.170	153	1450
50	3.222	5.159	154	1623
75	3.222	5.166	173	2040
100	3.224	5.171	174	1750

FE-SEM images for the mixed powder are shown in Figure 2a–f. In the raw powder product, the shape of the grains was quite dissimilar, and there was a precipitation of grains on the main grains. With the incorporation of fine crystals, the shape and average size of the grains changed but they were still uniformly distributed on the original particles. With the further increase in the fine crystal content, the original particles appeared with a larger size and were connected to each other. These fine crystals may be responsible for a good link between the grains and the homogenous distribution within the matrix. Generally, the particles appeared with two different sizes: micro- and nano-size. The micro-sized particles belong to the bulk ZnO phase, while the nano-sized ones belong to the fine crystal phase.

**Figure 2.** FE-SEM images of samples; (a) bulk-ZnO, (b) 10%, (c) 30%, (d) 50%, (e) 75%, and (f) 100% of fine crystals.

The average particle size (D) can be determined from the lineal intercept method using the equation $D = (1.56 L)/MN$, where L is the random line length, M is the magnification, and N is the number of grain boundaries intercepted by the lines on the micrograph [34]. The average particle size, listed in Table 1, ranged from 1277 to 2214 nm, which is eight times higher than the crystallite size obtained from XRD analysis. This variation can be explained by the FE-SEM images showing the plates containing multiple crystallites. The average crystallite and particle sizes are shown in Figure 3.

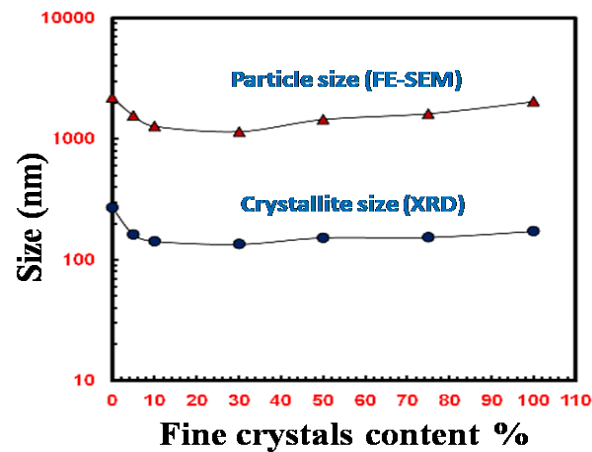


Figure 3. Average crystallite and particle sizes calculated from XRD and SEM versus fine crystals content.

3.2. I - V Characteristics

Figure 4 shows the I - V curves of the samples containing various concentrations of fine crystals. It is obvious from the I - V curves of the bulk ZnO that there are three regions; the first region and third one exhibit ohmic behavior, while the second region clearly shows nonlinear performance (upturn region). Additionally, this second region (nonlinear region) disappears for samples with ZnO fine crystals. This indicates that the potential barrier was completely deformed upon the addition of ZnO fine crystals even at very low doping contents (5%). The electric current densities generally shifted to higher values compared to those in the bulk sample. The breakdown field E_B is defined by the field applied when the current through the varistor is 1 mA/cm^2 [39,40]. The variation in E_B versus the fine crystal content is shown in Figure 5. The value of E_B decreased with the addition of ZnO fine crystals up to a content of 10%, followed by an increase with a content of 100%, but its value was generally lower than that for bulk-ZnO. This is, of course, logical and consistent with the absence of nonlinearity in the I - V curves for all the mixed phases.

The I - V relationship of a varistor is described by the following [38,39]:

$$J = (E/C)^\alpha \quad (2)$$

where J is the density of current, E is the electric field, C is a proportionality constant corresponding to the resistance of the ohmic resistor (nonlinear resistance), and α is the nonlinear coefficient ($\alpha = \log V / \log I$).

The value of α was calculated from the slope of the I - V curves plotted on a log scale, as described in [6]. Figure 6 shows the variation of α with doping percentage in three regions.

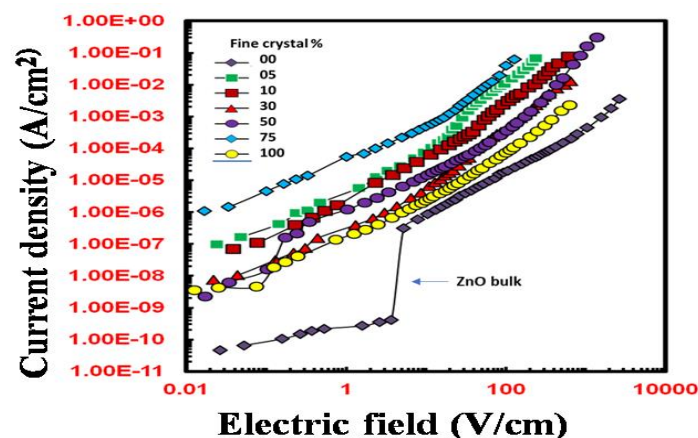


Figure 4. I - V characteristics for ZnO samples.

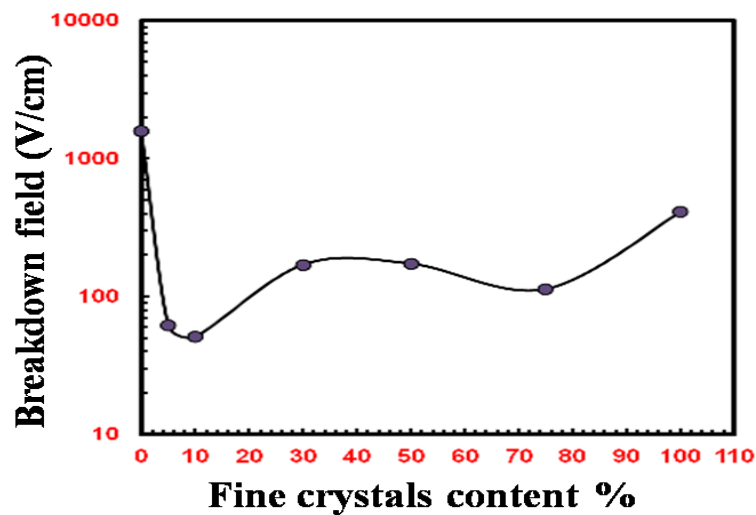


Figure 5. Breakdown field for ZnO samples.

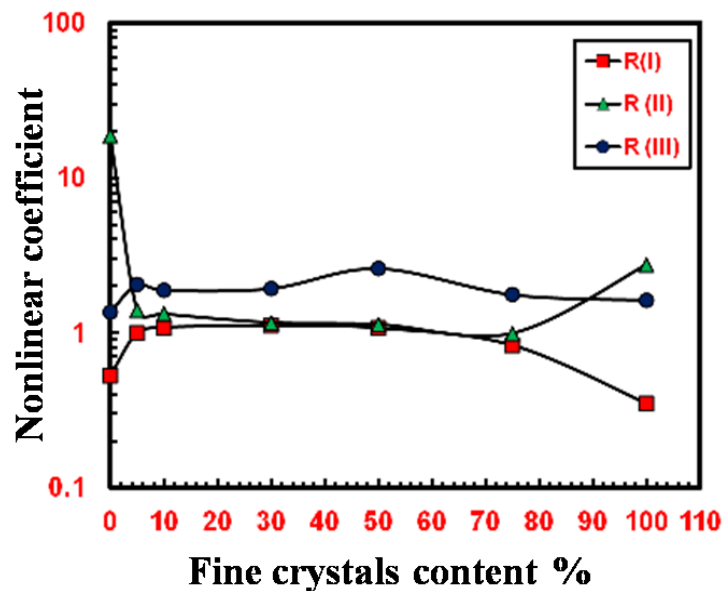


Figure 6. Nonlinear coefficient for ZnO samples.

Table 2 depicts a similar result. Apparently, the values of α decreased from 18.6 for the bulk phase and remained close to 1.5 for the samples with fine crystal percentages in the second region, which was also the same in the first and third regions. If one looks at the above results, one can see a good correlation between the crystallite size and nonlinear coefficient. Evidently, a non-ohmic feature of the bulk-ZnO varistor was suppressed upon adding ZnO fine crystals, shifting the breakdown fields to lower values.

Table 2. Breakdown field and nonlinear coefficient for bulk and mixed ZnO samples.

Fine Crystal Content (%)	E_B (V/cm)	α_1	α_2	α_3
0	1580	0.53	18.6	1.36
5	62	1.00	1.39	2.06
10	51	1.08	1.32	1.88
30	170	1.11	1.16	1.93
50	173	1.07	1.13	2.60
75	113	0.83	0.99	1.76
100	410	0.35	2.75	1.62

3.3. Electrical Conductivity

The electrical conductivity of the bulk and mixed phase ZnO was controlled by defects generated at high temperatures and the presence of doping, whether they were specifically added to the materials or not. During the cooling, defects may have migrated to the grain boundaries and disappeared (intrinsic defects) or accumulated if the solubility limit (extrinsic defects) was reached.

This process of migration is slow and thermally activated, indicating that defects near grain boundaries are efficiently eliminated at temperatures not much lower than the sintering temperature. Thus, the concentration affects the electrical properties of the ZnO varistor [34]. The samples were cooled to room temperature. Here, we assume that the defects were uniformly distributed in the materials at room temperature, and their concentration was the same as the concentration at sintering temperature, except for electrons and holes, which can easily spread at room temperature. Additionally, the electrical conductivity (σ) across the first ohmic region at room temperature was calculated using the relation $J = \sigma E$. The electrical conductivity for the ZnO varistors doped with ZnO fine crystals is shown in Figure 7 and in Table 3. Except for the 10% sample, it can be seen that σ is improved by fine crystal addition, in good agreement with the I - V measurements.

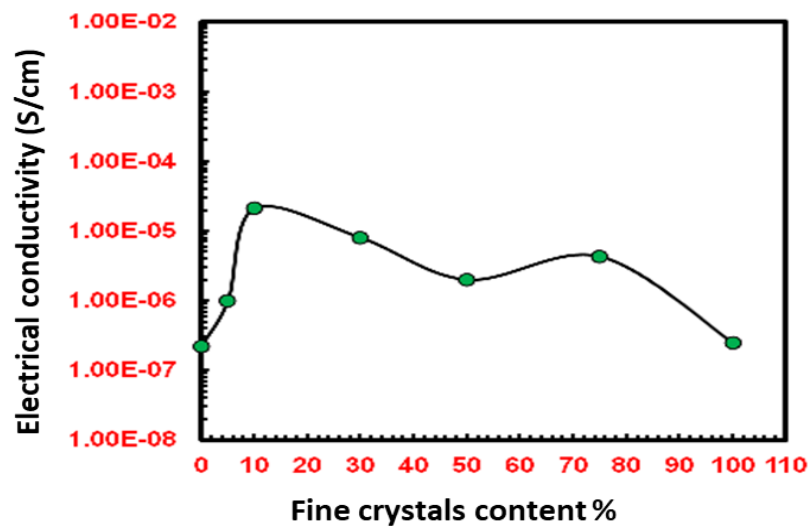


Figure 7. Electrical conductivity at room temperature for ZnO samples.

Table 3. Electrical conductivity and activation energy of ZnO samples.

Fine Crystal Content (%)	σ (S/cm)	E_a (meV) (300–420 K)	E_a (meV) (420–580 K)	E_a (meV) (580–620 K)
0	2.20×10^{-7}	128	374	815
5	1.02×10^{-6}	81	232	614
10	2.11×10^{-5}	33	38	398
30	8.00×10^{-6}	53	210	265
50	2.06×10^{-6}	17	228	447
75	4.31×10^{-6}	55	242	534
100	2.47×10^{-7}	164	369	811

The resistivity-versus-temperature measurements were performed at high-temperature ranges (300–620 K). From the values of resistivity, the electrical conductivities were calculated and are shown in Figure 8; the conductivity–temperature dependence was found to obey Athenian’s relation:

$$\Sigma = \sigma_0 \exp(-E_a)/(K_B T) \quad (3)$$

$$\ln \sigma = \ln \sigma_0 - 11.594 E_a (\text{eV})(1000/T) \quad (4)$$

where σ and σ_0 are the electrical conductivities at temperatures T and T_0 , respectively, and E_a is the activation energy. Evidently, σ increases with temperature for all samples. Through the temperature range chosen for the conductivity measurement, it was possible to differentiate the regions corresponding to various activation energies. The profile was separated into three regions according to the following temperature intervals: ($300 \text{ K} \leq T \leq 420 \text{ K}$), ($420 \text{ K} \leq T \leq 580 \text{ K}$), and ($580 \text{ K} \leq T \leq 620 \text{ K}$). The values of E_a were calculated from the slope of each plot by using the above logarithmic relation. Figure 9 shows the activation energy versus the ZnO nanoparticle doping content across the above three regions. Similar values are listed in Table 3. It is clear that E_a generally decreased with the addition of fine crystals up to 5%, followed by an increase upon increasing the fine crystal content to 100%. However, the values of E_a remain lower than those of the bulk ZnO sample.

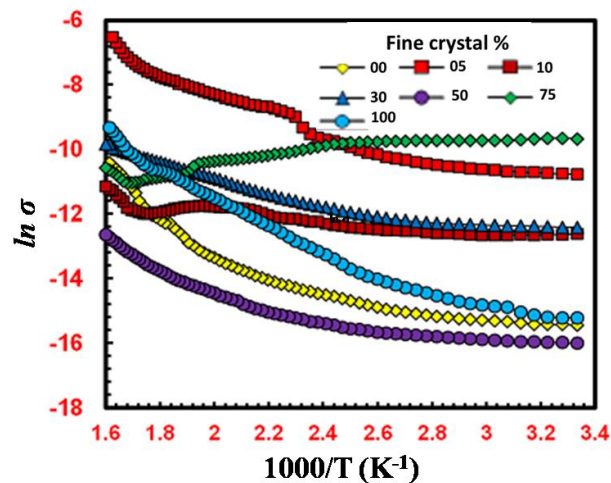


Figure 8. Plot of $\ln \sigma$ versus $1000/T$ for ZnO samples.

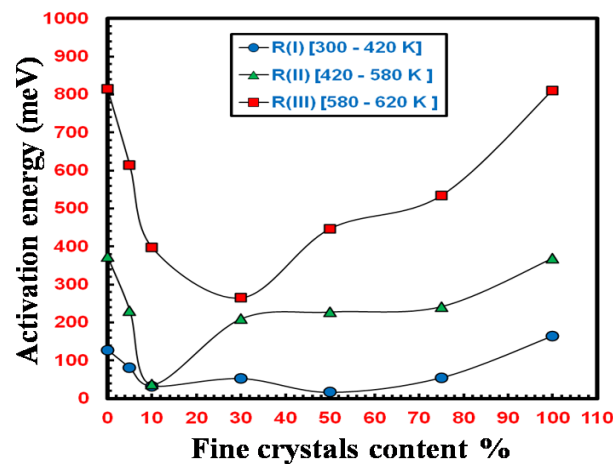


Figure 9. Activation energy for ZnO samples.

Decreasing the activation energy will decrease both the potential barrier and band gap. The interesting point here is that the values of E_a for the bulk-ZnO sample, in the second and third regions, are consistent with those obtained for the 100% fine crystal sample ($E_a = 128, 374,$ and 815 meV for the bulk sample, and $164, 369,$ and 811 meV for the 100% sample).

As compared to numerous previous investigations [41,42] based on microphase ZnO varistors, E_a varied between 500 and 1300 meV at high temperatures ($T > 673 \text{ K}$) and was less than 100 meV at low temperatures ($T > 373 \text{ K}$). These values are comparable to the data obtained for ZnO nanocrystalline compounds ($E_a = 570 \text{ meV}$) [41,42]. Furthermore, the behavior of E_a with the addition of ZnO fine crystals is similar to that of the grain size (Figure 2b).

Based on the above results, the probability of the ZnO fine crystals moving into the grain boundaries is considered to be very high at the sintering temperature. The nanosized crystals are able to localize at the edge of the grain and help in creating some other sensitive inter-grain conduction paths. The conduction paths can work in parallel [1,43] over the grain boundary and entirely deform the potential barrier that builds up between the grains. This is in good agreement with the I - V characteristics, where the linear behavior for the ZnO varistor is established. By contrast, a good correlation between the behaviors of the grain size, nonlinear coefficient, breakdown field, and activation energy with ZnO fine crystal addition can be reported.

Generally, the variations in the nature of the grain boundary and arrangement are well expected. In previous work, by measuring large numbers of individual grain boundaries, Einzinger et al. [44] reported that there can be considerable variation in the breakdown voltage from one boundary to another. They also showed that some boundaries were ohmic and some were nonlinear, while others were insulating. These results indicated above revealed that varistor properties closely depend on the microstructure features.

3.4. Discussion

Various efforts have made to present the fact that physiochemical properties of ZnO nanostructures can be strongly affected by the presence of deep and shallow defect-related in-gap states, which depend on the material's growth conditions. However, controlling the conductivity in ZnO has remained a major concern [45,46]. Even relatively small concentrations of native point defects and impurities (down to 10^{-14} cm⁻³ or 0.01 ppm) can significantly affect the electrical and optical properties of semiconductors [47–50]. Therefore, understanding the role of native point defects (i.e., vacancies, interstitials, and antisites) and the incorporation of impurities is key for controlling the conductivity in ZnO. For a long time, it has been postulated that the unintentional n-type conductivity in ZnO is caused by the presence of oxygen vacancies or zinc interstitials [51–53]. However, recent state-of-the-art density functional calculations corroborated by optically detected electron paramagnetic resonance measurements on high quality ZnO crystals have demonstrated that this attribution to native defects cannot be correct [54–60]. It has been shown that oxygen vacancies are actually deep donors and cannot contribute to n-type conductivity [56,59,60]. In addition, it was found that the other point defects (e.g., Zn interstitials and Zn antisites) are also unlikely causes of the observed n-type conductivity in as-grown ZnO crystals [57,58]. Instead, the cause would be related to the unintentional incorporation of impurities that act as shallow donors, such as hydrogen, which is present in almost all growth and processing environments [61,62].

4. Conclusions

In summary, the structure, I - V characteristics, and electrical conductivity dependence temperature of a bulk ZnO varistor modified with nanosized crystals of less than 200 nm are well studied, and their relationship has been established. It was observed that only average crystallite and particle sizes were affected by the addition of ZnO fine crystals; however, the hexagonal wurtzite structure of bulk ZnO ceramics remained unchanged. Different varistors were prepared with the bulk ZnO and bulk-mixed fine crystals of ZnO, and the electrical measurements of the varistors were performed under different conditions. As seen in the I - V characteristics, a linear behavior for mixed ZnO was observed. The non-linear region, breakdown field, and activation energy were found to decrease with the addition of ZnO fine crystals up to 10%, and then increased upon a further increase in fine crystals. However, the electrical conductivity measured at room temperature was improved and exhibited values higher than that of bulk ZnO. The values of the nonlinear coefficient decreased from 18.6 to 1.5 for the samples mixed with the fine crystals. Activation energy values of 128, 374, and 815 meV for the bulk sample and 164, 369, and 811 meV for the samples that contained 100% fine crystals for the three temperature regions of 300–420, 420–580, and 580–620 K, respectively, were obtained. Thus, nanosized crystals at grain boundaries of ZnO ceramics can fully deform the potential barriers of ZnO

varistors. The results obtained in this work might be helpful in elucidating the role of dopants in the nanoregime and establish the relationship between electrical and microstructural properties, which is a key requirement for a ZnO varistor.

Author Contributions: A.A. and A.S. played an equal role in preparing the samples, experimental work, data analysis, and results and discussion. A.A. and A.S. have read and approved the final manuscript. All authors have read and agreed to the published version of the manuscript.

Funding: This research was funded by the National Plan of Science, Technology and Innovation (MAARIFAH)—King Abdulaziz City for Science and Technology, the Kingdom of Saudi Arabia, grant number (08-NAN2-06). And The APC was funded by [08-NAN2-06].

Acknowledgments: This project was funded by the National Plan of Science, Technology and Innovation (MAARIFAH)—King Abdulaziz City for Science and Technology, the Kingdom of Saudi Arabia, (08-NAN2-06).

Conflicts of Interest: The authors declare that they have no conflict of interest.

References

1. Meng, P.; Yuan, C.; Xu, H.; Wan, S.; Xie, Q.; He, J.; Zhao, H.; Hu, J.; He, J. Improving the protective effect of surge arresters by optimizing the electrical property of ZnO varistors. *Electr. Power Syst. Res.* **2020**, *178*, 106041. [[CrossRef](#)]
2. Cao, W.; Xie, X.; Wang, Y.; Chen, M.; Qiao, Y.; Wang, P.; Zhang, Y.; Liu, J. Effect of Pr₆O₁₁ doping on the microstructure and electrical properties of ZnO varistors. *Ceram. Int.* **2019**, *45*, 24777–24783. [[CrossRef](#)]
3. Roy, S.; Roy, T.K.; Das, D. Grain growth kinetics of Er₂O₃ doped ZnO-V₂O₅ based varistor ceramics. *Ceram. Int.* **2019**, *45*, 24835–24850. [[CrossRef](#)]
4. Higashi, Y.; Koga, E. Barrier formation of single junctions with oxidation in SrCoO₃-doped ZnO varistors sintered in a reducing atmosphere. *J. Ceram. Soc. Jpn.* **2019**, *127*, 912–917. [[CrossRef](#)]
5. Dooho, C. The Transmittance Modulation of ZnO/Ag/ZnO Flexible Transparent Electrodes Fabricated by Magnetron Sputtering. *J. Nanosci. Nanotechnol.* **2020**, *20*, 379–383.
6. Huong, V.; Resende, N.J.; Fontanals, T.D.P.N.; Jiménez, C. Low-cost fabrication of flexible transparent electrodes based on Al doped ZnO and silver nanowire nanocomposites: Impact of the network density. *Nanoscale* **2019**, *11*, 12097.
7. Hsueh, T.J.; Peng, C.H.; Chen, W.S. A transparent ZnO nanowire MEMS gas sensor prepared by an ITO microheater. *Sens. Actuators B Chem.* **2020**, *304*, 127319. [[CrossRef](#)]
8. Zada, A.; Khan, M.; Qureshi, M.N.; Liu, S.; Wang, R. Accelerating photocatalytic hydrogen production and pollutant degradation by functionalizing g-C₃N₄ with SnO₂. *Front. Chem.* **2020**, *7*, 941. [[CrossRef](#)]
9. Lee, S.H.; Sohn, C.K.; Djafar, A. Electrical properties and microstructure of ZnO varistor with high surge protective characteristics. *J. Ceram. Process. Res.* **2019**, *20*, 164–168.
10. Obe, F.; Sato, Y.; Yamamoto, T.; Ikuhara, Y.; Sakuma, T. Current–voltage characteristics of cobalt-doped inversion boundaries in zinc oxide bicrystals. *J. Am. Ceram. Soc.* **2004**, *86*, 1616–1618. [[CrossRef](#)]
11. Zhou, Z.; Kato, K.; Komaki, T.; Yoshino, M.; Yukawa, H.; Morinaga, M.; Morita, K. Effects of dopants and hydrogen on the electrical conductivity of ZnO. *J. Eur. Ceram. Soc.* **2004**, *24*, 139–146. [[CrossRef](#)]
12. Gupta, T.K. Microstructural engineering through donor and acceptor doping in the grain and grain boundary of a polycrystalline semiconducting ceramic. *J. Mater. Res.* **1992**, *7*, 3280–3295. [[CrossRef](#)]
13. Inada, M. Formation mechanism of non-ohmic zinc oxide ceramics. *Jpn. J. Appl. Phys.* **1980**, *19*, 409. [[CrossRef](#)]
14. Olsson, E.; Dunlop, G.L.; Österlund, R. Development of functional microstructure during sintering of a ZnO varistor material. *J. Am. Ceram. Soc.* **1993**, *76*, 65–71. [[CrossRef](#)]
15. Nahmand, C.W.; Shin, B.C. Highly stable nonlinear properties of ZnO–Pr₆O₁₁–CoO–Cr₂O₃–Y₂O₃-based varistor ceramics. *Mater. Lett.* **2003**, *57*, 1322–1326.
16. Peiteado, M.; de la Rubia, M.A.; Velasco, M.J.; Valle, F.J.; Caballero, A.C. Bi₂O₃ vaporization from ZnO-based varistors. *J. Eur. Ceram. Soc.* **2005**, *25*, 1675–1680. [[CrossRef](#)]
17. Zada, A.; Muhammad, P.; Ahmad, W.; Hussain, Z.; Ali, S.; Khan, M.; Khan, Q.; Maqbool, M. Surface Plasmonic-Assisted Photocatalysis and Optoelectronic Devices with Noble Metal Nanocrystals: Design, Synthesis, and Applications. *Adv. Funct. Mater.* **2019**, *30*, 1906744. [[CrossRef](#)]

18. Qiabc, K.; Xinga, X.; Zada, A.; Li, M.; Wang, Q.; Liu, S.; Lin, H.; Wang, G. Transition metal doped ZnO nanoparticles with enhanced photocatalytic and antibacterial performances: Experimental and DFT studies. *Ceram. Int.* **2020**, *46*, 1494–1502.
19. Yamazaki, T.; Yamada, H.; Watanabe, K.; Mitsuishi, K.; Toda, Y.; Furuya, K.; Hashimoto, I. Nanoparticles in interlayers of Bi₂O₃-doped ZnO ceramics. *Surf. Sci.* **2005**, *583*, 166–172. [[CrossRef](#)]
20. Rodnyi, P.A.; Khodyuk, I.V. Optical and luminescence properties of zinc oxide (Review). *Opt. Spectrosc.* **2011**, *111*, 776–785. [[CrossRef](#)]
21. Tanigaki, T.; Kimura, S.; Tamura, N.; Kaito, C. A new preparation method of ZnO cubic phase particle and its IR spectrum. *Jpn. J. Appl. Phys.* **2002**, *41*, 5529–5532. [[CrossRef](#)]
22. Ino, S. Epitaxial growth of metals on rocksalt faces cleaved in vacuum. II. Orientation and structure of gold particles formed in ultrahigh vacuum. *J. Phys. Soc. Jpn.* **1966**, *21*, 346–362. [[CrossRef](#)]
23. Allpress, J.G.; Sanders, J.V. The structure and orientation of crystals in deposits of metals on mica. *Surf. Sci.* **1967**, *7*, 1–25. [[CrossRef](#)]
24. Kimoto, K.; Nishida, I. Multiply-twinned particles of F. C. C. metals produced by condensation in argon at low pressures. *J. Phys. Soc. Jpn.* **1967**, *22*, 940. [[CrossRef](#)]
25. Marks, L.D. Experimental studies of small particle structures. *Rep. Prog. Phys.* **1994**, *57*, 603–649. [[CrossRef](#)]
26. Saito, Y. Crystal structure and habit of silicon and germanium particles grown in argon gas. *J. Cryst. Growth* **1979**, *47*, 61–72. [[CrossRef](#)]
27. Iijima, S. Fine particles of silicon. I. Crystal growth of spherical particles of Si. *Jpn. J. Appl. Phys.* **1987**, *26*, 357–364. [[CrossRef](#)]
28. Dinesha, M.L.; Jayanna, H.S.; Ashoka, S.; Chandrappa, G.T. Temperature dependent electrical conductivity of Fe doped ZnO nanoparticles prepared by solution combustion method. *J. Alloys Comp.* **2009**, *485*, 538–541. [[CrossRef](#)]
29. Wurst, J.C.; Nelson, J.A. Lineal intercept technique for measuring grain size in two-phase polycrystalline ceramics. *J. Am. Ceram. Soc.* **1972**, *55*, 109. [[CrossRef](#)]
30. Bernik, S.; Daneu, N. Characteristics of ZnO-based varistor ceramics doped with Al₂O₃. *J. Eur. Ceram. Soc.* **2007**, *27*, 3161–3170. [[CrossRef](#)]
31. Carlson, W.G.; Gupta, T.K. Improved varistor nonlinearity via donor impurity doping. *J. Appl. Phys.* **1982**, *53*, 5746–5753. [[CrossRef](#)]
32. Gupta, T.K. Effect of minor doping on the high current application of the ZnO varistor. *Ferroelectrics* **1990**, *102*, 391–396. [[CrossRef](#)]
33. Fan, J.; Freer, R. The roles played by Ag and Al dopants in controlling the electrical properties of ZnO varistors. *J. Appl. Phys.* **1995**, *77*, 4795–4800. [[CrossRef](#)]
34. Han, J.; Mantas, P.Q.; Senos, A.M.R. Effect of Al and Mn doping on the electrical conductivity of ZnO. *J. Eur. Ceram. Soc.* **2001**, *21*, 1883–1886. [[CrossRef](#)]
35. Castro, M.S.; Aldao, C.M. Effects of the sintering temperature on the oxygen adsorption in ZnO ceramics. *J. Eur. Ceram. Soc.* **1999**, *19*, 511–515. [[CrossRef](#)]
36. Pei, G.; Xia, C.; Cao, S.; Zhang, J.; Wu, F.; Xu, J. Synthesis and magnetic properties of Ni-doped zinc oxide powders. *J. Magn. Magn. Mater.* **2006**, *302*, 340–342. [[CrossRef](#)]
37. Bates, C.H.; White, W.B.; Roy, R. New high-pressure polymorph of zinc oxide. *Science* **1962**, *137*, 993. [[CrossRef](#)]
38. Sedky, A.; Sawalha, A.A.; Yasien, A.M. Enhancement of electrical conductivity by Al-doped ZnO ceramic varistors. *Phys. B* **2009**, *404*, 3519–3524. [[CrossRef](#)]
39. Deshpande, V.V.; Patil, M.M.; Ravi, V. Low voltage varistors based on CeO₂. *Ceram. Int.* **2006**, *32*, 85–87. [[CrossRef](#)]
40. Houabes, M.; Bernik, S.; Talhi, C.; Bui, A. The effect of aluminium oxide on the residual voltage of ZnO varistors. *Ceram. Int.* **2005**, *31*, 783–789. [[CrossRef](#)]
41. Hahn, E.E. Some electrical properties of zinc oxide semiconductor. *J. Appl. Phys.* **1951**, *22*, 855. [[CrossRef](#)]
42. Heiland, G.; Mollwo, E.; Stöckmann, F. Electronic processes in zinc oxide. *Solid State Phys.* **1959**, *8*, 191–323.
43. Han, J.; Mantas, P.Q.; Senos, A.M.R. Defect chemistry and electrical characteristics of undoped and Mn-doped ZnO. *J. Eur. Ceram. Soc.* **2002**, *22*, 49–59. [[CrossRef](#)]
44. Einzinger, R. Grain junction properties of ZnO varistors. *Appl. Surf. Sci.* **1979**, *3*, 390. [[CrossRef](#)]

45. Janotti, A.; van de Walle, C.G. Fundamentals of zinc oxide as a semiconductor. *Rep. Prog. Phys.* **2009**, *72*, 126501. [[CrossRef](#)]
46. Szlachetko, J.; Kubas, A.; Cielak, A.M.; Sokoowski, K.; Makolski, L.; Czapla-Masztafiak, J.; Sa, J.; Lewinski, J. Hidden gapless states during thermal transformations of preorganized zinc alkoxides to zinc oxide nanocrystals. *Mater. Horiz.* **2018**. [[CrossRef](#)]
47. Lannoo, M.; Bourgoin, J. *Point Defects in Semiconductors I: Theoretical Aspects*; Springer: Berlin, Germany, 1981.
48. Lannoo, M.; Bourgoin, J. *Point Defects in Semiconductors II: Experimental Aspects*; Springer: Berlin, Germany, 1983.
49. Pantelides, S.T. (Ed.) *Deep Centers in Semiconductors: A State-of-the-Art Approach*, 2nd ed.; Gordon and Breach: Yverdon, Switzerland, 1992.
50. Stavola, M. (Ed.) *Identification of Defects in Semiconductors, Semiconductors and Semimetals*; Academic: San Diego, CA, USA, 1999; Volume 51.
51. Harrison, S.E. Conductivity and Hall effect of ZnO at low temperatures. *Phys. Rev.* **1954**, *93*, 52. [[CrossRef](#)]
52. Hutson, A.R. Hall effect studies of doped zinc oxide single crystals. *Phys. Rev.* **1957**, *108*, 222. [[CrossRef](#)]
53. Chen, X.; Zhang, Z.; Zhang, Y.; Yao, B.; Li, B.; Gong, Q. Passivation Mechanism of Nitrogen in ZnO under Different Oxygen Ambience. *Crystals* **2019**, *9*, 204. [[CrossRef](#)]
54. Kohan, A.F.; Ceder, G.; Morgan, D.; Van de Walle, C.G. First-principles study of native point defects in ZnO. *Phys. Rev. B* **2000**, *61*, 15019. [[CrossRef](#)]
55. Van de Walle, C.G. Defect analysis and engineering in ZnO. *Physica B* **2001**, *308*, 899. [[CrossRef](#)]
56. Janotti, A.; Van de Walle, C.G. Oxygen vacancies in ZnO. *Appl. Phys. Lett.* **2005**, *87*, 122102. [[CrossRef](#)]
57. Janotti, A.; Van de Walle, C.G. New insights into the role of native point defects in ZnO. *J. Cryst. Growth* **2006**, *287*, 58. [[CrossRef](#)]
58. Janotti, A.; Van de Walle, C.G. Native point defects in ZnO. *Phys. Rev. B* **2007**, *75*, 165202. [[CrossRef](#)]
59. Vlasenko, L.S.; Watkins, G.D. Optical detection of electron paramagnetic resonance for intrinsic defects produced in ZnO by 2.5-MeV electron irradiation in situ at 4.2 K. *Phys. Rev. B* **2005**, *72*, 035203. [[CrossRef](#)]
60. Vlasenko, L.S.; Watkins, G.D. Optical detection of electron paramagnetic resonance in room-temperature electron-irradiated ZnO. *Phys. Rev. B* **2005**, *71*, 125210. [[CrossRef](#)]
61. Van de Walle, C.G. Hydrogen as a cause of doping in zinc oxide. *Appl. Phys. Lett.* **2000**, *85*, 1012. [[CrossRef](#)]
62. Janotti, A.; Van de Walle, C.G. Hydrogen multicentre bonds. *Nat. Mater.* **2007**, *6*, 44. [[CrossRef](#)]



© 2020 by the authors. Licensee MDPI, Basel, Switzerland. This article is an open access article distributed under the terms and conditions of the Creative Commons Attribution (CC BY) license (<http://creativecommons.org/licenses/by/4.0/>).